

---

# END-TO-END LOCALIZED DEEP LEARNING FOR CRYO-ET

---

A PREPRINT

Vinith Kishore<sup>1</sup>, Valentin Debarnot<sup>3,1</sup>, Ricardo D. Righetto<sup>2</sup>, AmirEhsan Khorashadizadeh<sup>1</sup>, and Ivan Dokmanić<sup>1</sup>

<sup>1</sup>Department of Mathematics and Computer Science, University of Basel, 4051 Basel, Switzerland

<sup>2</sup>Biozentrum, University of Basel, 4056 Basel, Switzerland

<sup>3</sup>INSA-Lyon, Université Claude Bernard Lyon 1, CNRS, Inserm, CREATIS UMR 5220, U1294, LYON, France

\*Correspondence to: [ivan.dokmanic@unibas.ch](mailto:ivan.dokmanic@unibas.ch)

January 28, 2025

## ABSTRACT

Cryo-electron tomography (cryo-ET) enables 3D visualization of cellular environments. Accurate reconstruction of high-resolution volumes is complicated by the very low signal-to-noise ratio and a restricted range of sample tilts, creating a missing wedge of Fourier information. Recent self-supervised deep learning approaches, which post-process initial reconstructions done by filtered backprojection (FBP), have significantly improved reconstruction quality, but they are computationally expensive, demand large memory, and require retraining for each new dataset. End-to-end supervised learning is an appealing alternative but is impeded by the lack of ground truth and the large memory demands of high-resolution volumetric data. Training on synthetic data often leads to overfitting and poor generalization to real data, and, to date, no general end-to-end deep learning reconstructors exist for cryo-ET. In this work, we introduce CryoLithe, a local, memory-efficient reconstruction network that directly estimates the volume from an aligned tilt-series, overcoming the suboptimal FBP. We demonstrate that leveraging transform-domain locality makes our network robust to distribution shifts, enabling effective supervised training and giving excellent results on real data—without retraining or fine-tuning.<sup>1</sup>

**Keywords** cryogenic electron tomography, cryoET, missing wedge correction, denoising, sub-tomogram averaging, supervised learning, deep learning.

## 1 Introduction

Cryogenic electron tomography (cryo-ET) is an imaging technique that visualizes biological molecules and intracellular structures in their native 3D environments at nanometer resolution. In contrast to protein structure determination methods such as single-particle cryo-electron microscopy (cryo-EM), nuclear magnetic resonance (NMR), or X-ray crystallography—which require molecular isolation or crystallization—cryo-ET captures the full intracellular context that is crucial for understanding biological function. This bridges the gap between molecular imaging and whole-cell analysis, offering insights into cellular organization and dynamics [1].

Central to the progress of cryo-ET have been advancements in cryo-EM for which Jacques Dubochet, Joachim Frank and Richard Henderson were awarded the chemistry Nobel Prize in 2017 [2]. With the many improvements in sample preparation, microscopes, and reconstruction algorithms over the past decades [3], including automated pipelines for streamlined data acquisition and processing [4, 5], single-particle cryo-EM has today elucidated the structure of thousands of proteins at atomic resolution [6, 7, 8].

In practice, biological samples are vitrified and exposed to an electron beam to obtain measurements at a given sequence of tilt angles. The sample deteriorates with each exposure which limits the electron dose and results in a very

---

<sup>1</sup>This work was supported by the European Research Council Starting Grant 852821—SWING. Calculations were performed at sciCORE (<http://scicore.unibas.ch/>) scientific computing center at University of Basel.

poor signal-to-noise ratio. Early reconstruction algorithms such as the filtered backprojection (FBP) rely on analytic properties of the imaging operator [9, 10]. Recently self-supervised deep learning methods have proven very effective in denoising and improving such reconstructions. These methods can be trained with only noisy raw data, without noiseless ground truth required by supervised methods, and generally unavailable in biological imaging. Among the most popular is Cryo-CARE [11] which relies on the Noise2Noise framework [12]. Topaz-Denoise similarly uses Noise2Noise to train a general denoiser on a large set of volumes [13].

Beyond high noise, another challenge is that due to the sample geometry and tilt stage mechanics, the range of tilt angles is limited, typically between  $-60^\circ$  and  $60^\circ$ , with a step of  $2^\circ$  or  $3^\circ$ . This results in the notorious “missing wedge problem”—an unobserved wedge of information in the reciprocal Fourier space [14]—and to the corresponding missing wedge artifacts in the FBP reconstruction. A promising recent approach to the missing wedge problem is again by self-supervised learning which exploits the presence of cellular features such as proteins and membranes in random orientations within a tomogram. The first method to do this in cryo-ET is IsoNet which was shown to perform well in practice, especially when combined with a denoising algorithm [15]. The more recent DeepDeWedge approach jointly learns to denoise and correct the missing wedge, combining Noise2Noise and IsoNet-like approaches in a single framework [16].

We note that all the above denoising and missing wedge correction approaches are post-processing methods. They are applied to the initial reconstructions obtained by filtered back-projection (FBP). The fixed FBP, however, is a suboptimal step which introduces delocalized artifacts and spatially correlated noise [17].

The development of supervised methods for cryo-ET is stymied by the absence of ground truth data. In an attempt to get around this problem, several simulators have been created to generate realistic data. They leverage known structures from the protein data bank [18] to create protein-dense synthetic volumes. These simulators have been used in deep learning methods for segmentation of membranes [19, 20], for template matching [21], and to train tomogram denoising networks [22]. But using simulated volumes to train reconstruction networks has been hampered by the complexity of the full cryo-ET forward model and the inadequate approximation of real cellular volumes by simple distributions of proteins. Training on simulated volumes and measurements generalizes poorly to complex, messy real data.

In this work, we show that supervised learning can in fact lead to high-quality reconstructions on real data. We introduce a coordinate-based framework to recover the volumes directly from the projections, thus avoiding the suboptimal FBP reconstruction as the starting point. The main challenges in applying *end-to-end* supervised learning to cryo-ET are 1) the lack of ground truth data and overfitting to simulations and 2) the high memory demands of the 3D volumes and projections. Here we propose two ideas to address these challenges:

- We design a local reconstruction algorithm which only uses a small subset of observed projections to reconstruct the volume at a given coordinate. This coordinate-based design enables memory-efficient training well-suited for 3D reconstruction of large volumes. We build on the recent GLIMPSE framework of Khorashadizadeh *et al.* [23] who showed that such coordinate-based local reconstruction networks give excellent out-of-distribution generalization in 2D computed tomography (CT).
- We carefully design a bespoke training set by combining several packages to obtain denoised, missing-wedge corrected tomograms from real data. We select only a small subset of the processed tilt-series that gives the highest-quality reconstructions that will serve as training targets. We show that the proposed local reconstruction network, thanks to its robustness to distribution shifts, generalizes to unseen data and gives high-quality reconstructions on real data, while being much faster than related self-supervised methods.

The proposed cryo-ET reconstruction algorithm directly processes aligned tilt series and produces a denoised, missing-wedge-corrected tomogram. Transform-domain locality greatly reduces the memory footprint and enables end-to-end training, resulting in the first general-purpose neural network for cryo-ET reconstruction that can be used off-the-shelf to process any aligned tilt series. There is no need for experiment-specific training as generally in self-supervised methods. Locality enables supervised learning on existing reconstructions without overfitting. Since we do not post-process the FBP output, we can, in principle, perform statistically optimal inference directly from raw data. We demonstrate CryoLite on both real and simulated data, the latter allowing us to precisely quantify the quality of reconstructions. In particular, we show that once trained, CryoLite performs consistently on qualitatively distinct test volume distributions.

As detailed in the associated Github page<sup>2</sup>, we will continuously improve and release our pre-trained models, allowing straightforward reconstructions directly from aligned tilt series by running a few lines of Python code. We will also publish our training data to facilitate the development of new deep learning algorithms for cryo-ET.

<sup>2</sup><https://github.com/swing-research/CryoLite>

## 2 Related work

**Cryo-ET data acquisition and processing** The first step of the tomography pipeline is to collect the tilt series of the sample. For biological samples, the specimen is first cryogenically fixed by vitrification [24, 25]. Vitrified samples are exposed to an electron beam of known dosage, and the electrons that pass through the sample are observed using a direct electron detector [26]. Since electrons damage the sample the dose must be kept low, resulting in poor signal-to-noise ratio (SNR) [27, 28]. Multiple short-exposure snapshots are recorded at each tilt and aligned and averaged to account for sample drift [29]. Averaged frames are exposure-weighted to create a projection image [30]. Measurements are affected by the contrast transfer function (CTF) which depends on the optical parameters of the microscope, usually estimated post-acquisition [31]. The sample moves and deforms between tilts so the tilt series must be aligned. For purified specimens (e.g. viruses and other large macromolecules) this can be done by adding fiducial markers such as gold beads to the sample, but for cellular specimens a patch tracking approach is typically used [32], with varying degrees of user intervention required to obtain a successful alignment. Recently, fully automated tools based on cross-correlation approaches [33] or deep neural networks which leverage the spatial and spectral regularity of volumes [34] have been proposed. Here, we assume that well-aligned tilt series are available, regardless of how they were obtained.

**Denoising and missing wedge correction** Classic approaches to 3D tomography include iterative least squares (ILS), algebraic reconstruction technique (ART) [35], simultaneous iterative reconstruction technique (SIRT) [36] or, most commonly, FBP [37]. At low SNR, FBP amplifies noise and results in poor reconstruction quality. Many denoising techniques have been adapted for cryo-ET, including Wiener filtering, multiscale methods [38], bilateral filtering [39], iterative median filtering [40], and nonlinear anisotropic diffusion [41], to name a few. Self-supervised deep learning techniques like Cryo-CARE [11] denoise tomograms by splitting the measurements into two sets, constructing two noisy tomograms, and training a U-Net to recover one from the other. Generalization is limited so this must be done for each new tilt series or at least for each new sample and acquisition session. Topaz-Denoise [13] attempts to obviate this by self-supervised learning from a large collection of noisy tomograms, but again, with limited generalization ability. Moreover, the missing wedge further deteriorates the quality of reconstructions. IsoNet exploits the geometry in cryo-ET [15] to postprocess sub-volumes of the FBP reconstruction to correct for the missing wedge. Its main limitation is that it is strongly influenced by the quality of the input. In practice, it is often combined with denoisers like Cryo-CARE or *ad hoc* Wiener filtering. DeepDeWedge [16] combines the Noise2Noise idea with rotational equivariance to consistently fill the missing wedge. It yields reconstructions which appear significantly sharper than using IsoNet alone, at the price of needing two sets of independent measurements as input, like Cryo-CARE. Both IsoNet and DeepDeWedge typically process the FBP output, which is degraded by correlated noise and missing wedge artifacts.

Several methods combine neural fields (also known as implicit neural networks) developed for differentiable rendering [42, 43] with the projection forward model to recover the volumes from the projections in cryo-ET [44, 34, 45]. The volume is represented using a neural field instead of a grid, which helps to reduce artifacts due to the missing wedge. This is commonly assumed to be due to the implicit bias of neural networks. However, like IsoNet and DeepDeWedge, these networks have to be trained separately for each reconstruction, and the theoretical basis for regularization is unclear.

**Data simulators** Several tools have been developed to create realistic artificial cellular volumes and simulate the acquisition process. Purnell *et. al.* [22] developed a tool to simulate realistic-looking crowded bio-environments using solved structures in the Protein Data Bank [18]. They provide tools to generate various types of protein assemblies, membrane complexes, and molecule distributions. Polnet *et. al.* [19] simulates cellular environments with a focus on curved filaments decorated with various biomolecules. Parakeet [46] generates high-resolution crowded environments. There exists a plethora of accurate forward model implementations [47, 48, 49, 50, 46]. Simulation data has been used to train neural networks on downstream tasks, including segmentation of membranes [19, 20] and template matching [21]. Purnell *et. al.* [22] also provides an example of simulating volumes that look similar to the acquisition data to train a tomogram denoising U-Net, which they use to reconstruct filaments in real data.

**Local reconstruction methods** FBP produces global streak artifacts due to sparse orientation sampling and missing wedge (see, e.g., Figure 4d). For reconstruction methods processing patches, it is challenging to remove streak artifacts emanating from an object not in the processed patch without overfitting (as there could be similarly structured real features). Since processing the entire reconstructed volume is computationally prohibitive, an alternative is to process directly the projections. In this case, it is possible to establish a notion of locality: a point source in the volume affects only one line in each projection. This has been exploited in two-dimensional tomography [51, 52, 53, 54]. Our approach builds on GLIMPSE [23], a supervised learning framework for 2D CT that builds a lightweight, efficient architecture robust to changes in distribution between training and evaluation. The training efficiency and strong generalization of

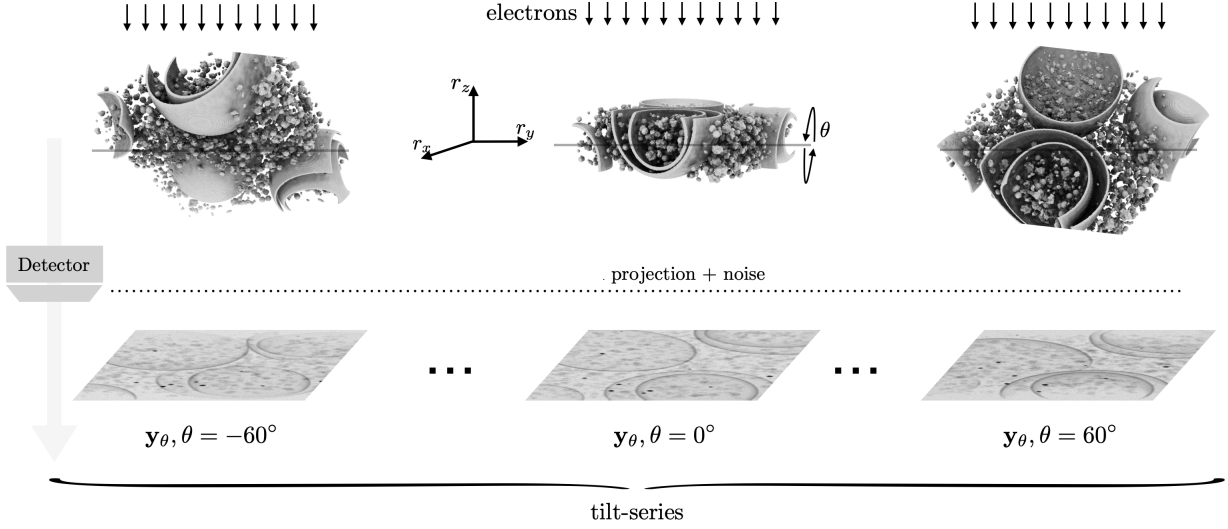


Figure 1: Illustration of the cryo-ET acquisition process.

local coordinate-based networks are explored in [55, 56] for various image reconstruction tasks. We finally mention related works applying MLPs patchwise in image classification [57] and processing [58] tasks.

### 3 Methods

In this section, we show how cryo-ET imaging can be seen as a local operation after a simple 1D filtering. This allows us to build a lightweight neural network that only uses a fraction of the tilt-series to predict the value of a given pixel in the tomogram.

#### 3.1 Image formation model

We will assume that the effect of the CTF is negligible at the given sampling rate (e.g. after downsampling or "binning" operations), or has already been corrected in the 2D tilt-series [31, 59, 60]. This means that we work under the projection approximation and weak phase-object assumptions, which are valid to reach the current reconstruction resolutions [61].

The unknown volume density  $V : \mathbb{R}^3 \rightarrow \mathbb{R}$  has to be estimated from its noisy tilt-series  $\{y^\theta\}_{\theta=\theta_{\min}}^{\theta_{\max}}$ . Letting  $\mathbf{r} = (r_x, r_y, r_z)$ , the noiseless tilt-series can be modeled as

$$y_\theta^*(r_x, r_y) = \int V(\mathbf{R}_\theta \mathbf{r}) dr_z, \quad (1)$$

where  $\mathbf{R}_\theta(\cdot)$  is the 3D rotation matrix around the second axis,

$$\mathbf{R}_\theta = \begin{bmatrix} \cos(\theta) & 0 & \sin(\theta) \\ 0 & 1 & 0 \\ -\sin(\theta) & 0 & \cos(\theta) \end{bmatrix},$$

where  $\theta$  is the rotation angle. The tilt angles  $\theta$  are typically constrained between  $-60$  and  $+60$  degrees, with a 2 or 3 degree spacing determined by the maximum dose. We observe discretized, noisy projections  $\mathbf{y}_\theta \in \mathbb{R}^{n_1 \times n_2}$ , given by

$$\mathbf{y}_\theta[i, j] \approx [b * y_\theta^*](\Delta_x i, \Delta_y j) + \epsilon[i, j], \quad (2)$$

where  $b$  is a sampling kernel modeling the finite pixel size,  $\epsilon[i, j]$  is noise typically modeled as additive white Gaussian noise, and  $\Delta_x, \Delta_y$  are the pixel dimensions on the sensor. The cryo-ET acquisition process is illustrated in Figure 1.

#### 3.2 Local properties of the impulse response of the tomography operator

The above projection operator has the property that a point in the volume influences only one point in each tilt. As in [23], this can be understood by considering how a point source  $V(\mathbf{r}) = \delta(\mathbf{r} - \mathbf{r}^0)$  is transformed, with  $\delta$  being the

Dirac delta. In this case, for any  $(r_x, r_y) \in \mathbb{R}^2$  and any projection angle  $\theta \in [-\pi, \pi)$ , the noiseless projections are given by

$$y_\theta(r_x, r_y) = \int \delta(\mathbf{R}_\theta \mathbf{r} - \mathbf{r}^0) dr_z \quad \text{where } \mathbf{r} = (r_x, r_y, r_z)^T$$

which formally yields

$$y_\theta(r_x, r_y) = \delta(r_x - (r_x^0 \cos(\theta) - r_z^0 \sin(\theta)), r_y - r_y^0). \quad (3)$$

This means that a point source influences the intensity of the tilt-series along the curve

$$\theta \mapsto \mathbf{r}_\theta(\mathbf{r}^0) = (r_x^0 \cos(\theta) - r_z^0 \sin(\theta), r_y^0), \quad (4)$$

which is a sinusoid in  $\theta$ . Thus, in principle, all the information of the volume from location  $\mathbf{r}^0$  is present at the points  $\mathbf{r}_\theta$  in the projections. We note that the points on the curve  $\mathbf{r}_\theta$  are also influenced by other points in the volume. This mixing can be partially undone using a simple filter along the  $x$  analogous to the ‘‘filtering’’ step of the FBP; we elaborate on this below.

In this paper, we exploit the local support of the impulse response of the cryo-ET projection operator to build a reconstruction method that uses only a small subset of the tilt series around  $\mathbf{r}_\theta(\mathbf{r}^0)$  to estimate  $V(\mathbf{r}^0)$ . Our goal is thus, loosely speaking, to invert the mapping  $V(\mathbf{r}) = \delta(\mathbf{r} - \mathbf{r}^0) \mapsto (y_\theta(\mathbf{r}_\theta))_\theta$ . This mapping is generally not invertible due to the missing wedge and the sparse sampling of the tilt angles. To overcome this problem, we propose a local neural network to approximate the inverse.

Using only  $(y_\theta(\mathbf{r}_\theta))_\theta$  as input to the inversion network has the advantage of drastically reducing the dimension of the inversion problem. However, it amounts to assume that there is no correlation between pixels of the tilt-series and becomes suboptimal in the presence of noise. For this reason, we consider measurements in a neighborhood which is a ‘‘thickening’’ of  $\mathbf{r}_\theta$ . This reflects the fact that the strong correlations in the data are primarily local, and only these local correlations can be robustly estimated from finite data, while still greatly reducing the computational and statistical complexity of learning the inverse. The specific architecture of the neural network is described in Section 3.4.

### 3.3 Transform-localized training

In this section we detail the patch extraction procedure. We let  $N$  denote the number of projections in the tilt-series,  $M \times M$  be the size of the projections<sup>3</sup> and  $P \times P$  be the size of the patch of measurements extracted from the tilt-series. Note that the number of projection angles is fixed for simplicity, but is not an intrinsic limitation of the proposed approach.

In order to estimate the volume density at given position  $\mathbf{r} \in \mathbb{R}^3$ , CryoLite processes an  $N \times P \times P$  dimensional input through a neural network. We let  $f_\gamma : \mathbb{R}^{N \times P \times P} \rightarrow \mathbb{R}$  denote the neural network with  $\gamma \in \mathbb{R}^K$  its  $K$  learnable parameters. As mentioned above, a simple 1D convolutional filtering along the  $x$  coordinate localizes information in a similar way that the filtering step of the FBP does. Intuitively, it is a way to incorporate global information in the reconstruction in a way which does not lead to overfitting. In practice, we use the cosine ramp filter, a high-pass filter with a large receptive field similar to the ramp filter used in FBP, see Section 3.5. We let  $\hat{\mathbf{y}}$  denote the filtered projections.

The neural network  $f_\gamma$  is trained using  $L$  paired training examples composed of  $L$  filtered tilt-series and their corresponding volume densities  $\{(\hat{\mathbf{y}}_l, V_l)\}_{l=1}^L$ , by approximately solving

$$\min_{\gamma} \mathbb{E}_{V, \mathbf{y}, \mathbf{r}} \|V(\mathbf{r}) - f_\gamma(\mathbf{p})\|^2, \quad \mathbf{p} = [C(\hat{\mathbf{y}}_{\theta_1}, r_{\theta_1}(\mathbf{r})), \dots, C(\hat{\mathbf{y}}_{\theta_N}, r_{\theta_N}(\mathbf{r}))], \quad (5)$$

where the cropping operator  $C(\cdot, \cdot)$  is defined in Equation (6)

We use Adam [62] optimizer to minimize the cost function. In particular, we sample the expectation by taking batch over the finite number of volumes density available, but also pixels, which allows to trade-off training time for GPU memory and enables training on large volumes.

More precisely, for each volume, we first sample target locations in the volume at random. Our network outputs the value of the estimated volume at arbitrary real coordinates, so the sampled locations need not lie on a fixed grid. Then, we extract the corresponding patches from the tilt-series to serve as input of CryoLite’s neural network, as illustrated in Figure 2. Finally, we evaluate the cost function defined in Equation (5) and use automatic differentiation to update the learnable parameters.

<sup>3</sup>For notational simplicity we only consider square projections, but non-square tilt-series are easily handled.

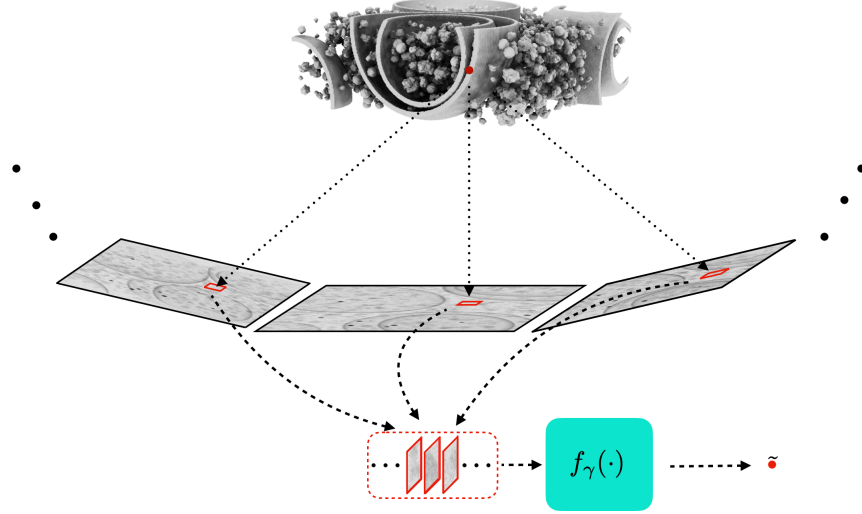


Figure 2: Illustration of the local patch extractor. The figure highlights the part of the projections where the volume at a particular location (red dot) is observed. CryoLiteh extracts a local patch around these locations, which is processed by a neural network.

The patch extraction is formally defined by the cropping operator  $C(\cdot, \cdot)$ , which takes a projection  $\mathbf{y}_\theta$  and the locations of the projections  $\mathbf{r}^0$  and crops a patch around these projections,

$$C(\hat{\mathbf{y}}_\theta, \mathbf{r}^0)[i, j] = \hat{\mathbf{y}}_\theta \left( \mathbf{r}_\theta(\mathbf{r}^0) - \Delta \begin{bmatrix} i \\ j \end{bmatrix} \right), \quad i, j \in \left( - \left\lfloor \frac{P}{2} \right\rfloor, \left\lfloor \frac{P}{2} \right\rfloor \right), \quad (6)$$

where  $\Delta$  depends on the resolution of the projection and  $\mathbf{r}_\theta(\mathbf{r}^0)$  is given by Equation (4). We use bilinear interpolation to estimate the projection values if the sampling location is not on the discrete grid.

### 3.4 Architecture

The base block of the neural network architecture consists of standard MLPs (multi-layer perceptrons), defined as

$$\text{MLP} : \mathbb{R}^{N P^2} \ni x \mapsto W_{\text{out}} \text{ReLU}(W_H \text{ReLU}(W_{H-1} \dots \text{ReLU}(W_{\text{in}}(x))))),$$

where ReLU is the rectified linear unit,  $W_{\text{in}} \in \mathbb{R}^{N P^2 \times \text{hidden}}$ ,  $W_i \in \mathbb{R}^{\text{hidden} \times \text{hidden}}$  and  $W_{\text{out}} \in \mathbb{R}^{1 \times \text{hidden}}$ . The input vector is always of dimension  $P^2 N$  (after being flattened), and the output always of dimension 1. It remains to select the hidden dimension and number of layers  $H$  which are treated as hyperparameters. Note that we use linear layers without bias. This has been shown to improve robustness to noise [63]. Moreover, it results in scaling equivariant (1-homogenous) networks which greatly facilitates handling different normalizations of volumes and data.

An important advantage of our transform-domain local approach is that we can build a true 3D reconstructor which optimally exploits the 3D correlation structure of the measurement data and the volumes. Doing this naively, however, still results in high compute and memory complexity. We thus exploit the structure of the cryo-ET forward model in Equation (3) and combine MLPs which operate on constant- $y$  slices with an MLP acting along the  $y$  dimension.

We split the patches along the rotation axis to obtain  $P$  vectors of dimension  $N \times P$ . Each of these  $P$  vectors is processed by an MLP; we denote by  $\text{MLP}_s$  the MLP that processes the  $s$ th vector. These MLPs output a vector of slice features of dimension  $F \ll NP$  which helps reduce the computational burden. These feature vectors are then concatenated and processed by a second MLP denoted  $\overline{\text{MLP}}$ . Figure 3 shows the schematic diagram of the network acting on the projections.

More formally, let  $\text{MLP}_s(\cdot) : \mathbb{R}^{P \times N} \rightarrow \mathbb{R}^F$  for  $1 \leq s \leq P$  and  $\overline{\text{MLP}} : \mathbb{R}^{P \times F} \rightarrow \mathbb{R}$ . The overall neural network  $f_\gamma$  can be written as

$$f_\gamma(\mathbf{p}) = \overline{\text{MLP}}([\text{MLP}_1(\mathbf{p}_1), \text{MLP}_2(\mathbf{p}_2), \dots, \text{MLP}_P(\mathbf{p}_P)]),$$

where  $p_s$  denotes the  $s$ -th slice of the tilt-series patch and the learnable weights  $\gamma$  are the concatenation of all the learnable parameters of the different MLPs.

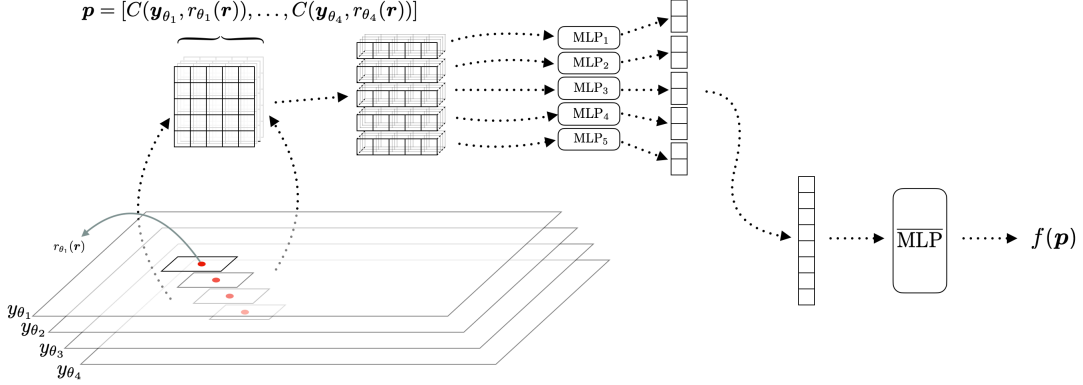


Figure 3: Schematic diagram of the SliceMLP architecture. The patches are grouped along the slices based on the axis of the tilt-series. These slices are fed into the corresponds MLPs ( $MLP_i$ ) to obtain a feature vector, which is used by a combination MLP ( $\overline{MLP}$ ) to estimate the volume at a particular location  $r$ . While the architecture appears slicewise for computational reasons, it is fundamentally a 3D architecture that exploits the 3D correlation structure of the measurement data to recover the volume.

### 3.5 Link between CryoLithe and Filtered Back-Projection

The FBP is arguably the most used reconstruction algorithm in cryo-ET. It is simple, fast, and can handle moderate noise. However, in the limited-angle setting (and due to incomplete sampling of accessible angles) of cryo-ET, the FBP generates streak-like artifacts and renders details at certain orientations invisible. Figure 4d shows slices of the FBP reconstruction, compared with the corresponding reference slices in Figure 4c. Because of the limited-angle setting and the presence of additive Gaussian noise in the tilt-series, we observe that the contrast between the particle and the background is low, and the resolution is poor due to artifacts.

In practice, the filter is chosen empirically among several high-pass filters, such as the ramp filter. Then, the filtered projection is backprojected to reconstruct the 3D volume. Let  $\hat{y}_\theta(r_x, r_y)$  denote the filtered projection. The FBP volume reconstruction is

$$\hat{V}_{\text{FBP}}(r_x, r_y, r_z) = \int_{\theta} \hat{y}_\theta(r_x \cos(\theta) - r_z \sin(\theta), r_y) d\theta = \int_{\theta} \hat{y}_\theta(\mathbf{r}_\theta) d\theta. \quad (7)$$

Our proposed approach can then be seen as a nonlinear generalization of the FBP, where the integral (the average) along the sinusoidal support is replaced by a learnable function parameterized by a neural network. In contrast to FBP, CryoLithe uses a neural network in order to optimally process the local measurements. This also underlines that CryoLithe is an approach to deep learning for cryo-ET which is substantially different from the existing postprocessing methods.

## 4 Results

We now demonstrate CryoLithe on a series of experiments. First, we study the case where CryoLithe is trained on simulated data. This allows us to precisely assess performance and compare with existing approaches. Second, we address the case of real data by training on a carefully curated experimental dataset. We show that this enables CryoLithe to achieve strong results on different types of real experimental data.

### 4.1 Training with simulated tomograms

We combine two simulation tools—cryo-TomoSim [22] and tomosipo [64]—to generate clean tomograms and simulate the acquisition of tilt-series. Cryo-TomoSim is used to generate 48 volumes of size  $800 \times 800 \times 400$  voxels at  $6\text{\AA}$  resolution containing proteins from the protein data bank [65]. We selected all proteins that have been resolved to resolution better than  $2\text{\AA}$  (about 1000). We select a subset of these proteins to generate each volume. We generate noiseless tilt-series with 41 projections of size  $800 \times 800$  pixels (tilt range from  $-60^\circ$  to  $60^\circ$ , step size  $3^\circ$ ) using tomosipo [64]. We add white Gaussian noise to obtain a signal-to-noise ratio (SNR) of  $-5\text{dB}$ . Figures 4a and 4b show the  $0^\circ$  projection respectively without noise and with  $-5\text{dB}$  noise.

Next, we train the multi-slice architecture presented in Section 3.4 with a hidden layer size of 512 and a depth of 5. We sample patches of size  $21 \times 21$  and sample 10000 reference points at random from the volumes and the corresponding patches from the tilt-series. We fit the network parameters using the mean squared error and Adam optimizer with a

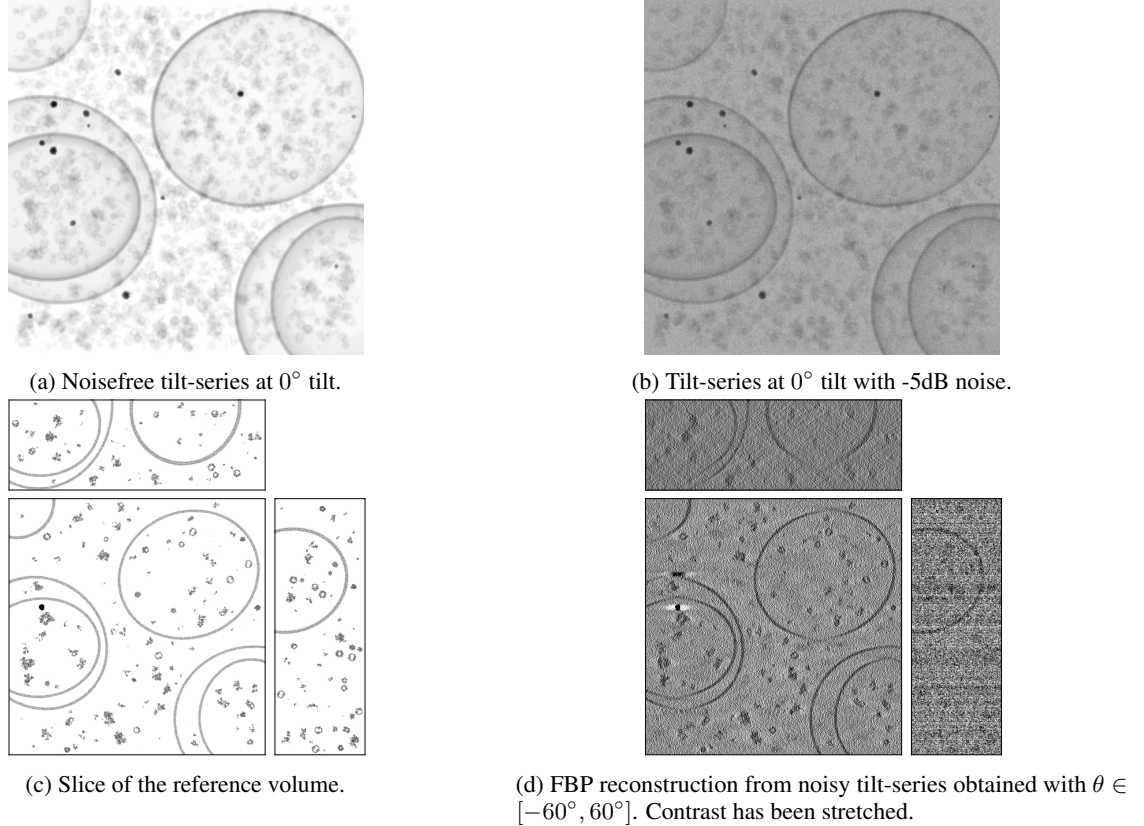


Figure 4: FBP reconstruction produces streak artifacts which limit the resolution in particular along the  $z$ -axis. FBP reconstruction is used as input of most denoising and missing-wedge correction algorithms.

learning rate of  $10^{-4}$  over 1000 epochs. We note that the model looks at 0.004% of the volume at each epoch which means that even after 1000 epochs, only a small proportion of the pixels of the ground truth volumes have been explicitly used.

#### 4.1.1 Reconstruction on simulated tilt-series

We first evaluate the trained model on a simulated test volume similar to the one used for training (using cryo-TomoSim and the same protein dataset). Results are shown in Figure 5. We measure the quality of the reconstruction using Fourier shell correlation (FSC) [66]. The FSC between two discrete volumes  $\rho$ ,  $\rho'$  at a radius  $r$  of the shell is defined as

$$\text{FSC}(\rho, \rho')[r] = \frac{\sum_{|\xi|=r} \widehat{\rho}(\xi) \widehat{\rho}'(\xi)}{\sqrt{\sum_{|\xi|=r} \widehat{\rho}(\xi)^2 \sum_{|\xi|=r} \widehat{\rho}'(\xi)^2}}, \quad (8)$$

where  $\widehat{\rho}$  (resp.  $\widehat{\rho}'$ ) denotes the three-dimensional Fourier transform of the discrete volume  $\rho$  (resp.  $\rho'$ ). The FSC measures the correlation between the estimated and the original volume per frequency magnitude, giving information about the resolution to which information can be recovered in the estimated volume.

The inference time of competing reconstruction methods is reported in Table 1. Experimental parameters used to generate this table are reported in Appendix A. Since CryoLite relies on supervised training, it is considerably faster. Obviously, CryoLite requires many hours of training, but once trained it can be applied as-is to arbitrary data; we release pre-trained models on the Github page<sup>4</sup>. Visually, CryoLite produces results comparable to self-supervised methods, but faster as it requires no training per inference. The FSC curve of CryoLite in Figure 5g is similar to those of FBP+Cryo-CARE+IsoNet and FBP+DeepDeWedge. In Figures 5h and 5i we report the FSC restricted to the visible wedge (i.e., the task is to denoise and compensate the sparse views), and the FSC restricted to the missing wedge (i.e., the task is to extrapolate). While the denoising performance of the different methods is comparable (Figure

<sup>4</sup><https://github.com/swing-research/CryoLite>



5h), the missing wedge compensation is best with FBP+Cryo-CARE+IsoNet, FBP+DeepDeWedge and CryoLithe, as expected. For this reason, we will focus on these three methods in the following experiments. The bad performance of FBP+IsoNet is also expected, as IsoNet should be run on high-contrast, pre-denoised tomograms. We include this result so that the denoising and missing-wedge restoration capabilities can be decoupled.

In order to validate the robustness of CryoLithe to out-of-distribution data, we now test it on tilt-series obtained with volumes from the SHREC dataset [67]. SHREC contains simulated volumes with randomly placed proteins, vesicles, and gold fiducials, and is commonly used for benchmarking classification and localization tasks in cryo-ET. We generate projections as described previously and use the network trained on the cryo-TomoSim simulations. Figure 6 shows the orthogonal slices of the reconstruction and FSC curve. From Figures 5 and 6, under similar observation conditions, the reconstruction performance remains comparable to that of the test volume, demonstrating that the network reconstructs the volume without introducing artifacts or hallucinations despite the distribution shift. The FSC curves under different conditions in Figures 6d, 6e and 6f show that the performance of CryoLithe follows that of FBP+Cryo-CARE+IsoNet which is the state of the art self-supervised reconstruction pipeline. We emphasize that FBP+Cryo-CARE+IsoNet is trained specifically for this one example whereas CryoLithe has been trained beforehand on a completely different dataset and is applied off-the-shelf to efficiently reconstruct the tomogram.

FBP+Cryo-CARE	FBP+IsoNet	FBP+Cryo-CARE + IsoNet	FBP+DeepDeWedge	CryoLithe
1:14:36	3:58:24	5:13:00	17:03:09	0:38:28

Table 1: Run time of the different methods in hours:minutes:seconds format for processing a tilt-series of size  $41 \times 800 \times 800$  into a tomogram of size  $800 \times 800 \times 400$ .

#### 4.1.2 Ablation study

We now study the effect of the various hyperparameters in CryoLithe using simulated data for training and testing. We are interested in the relative differences between the different settings so we only reconstruct part of the volume to compute the metrics. Further, for computational efficiency, the volume is evaluated on a grid that is coarser from that of the original tomograms by a factor of 4 in each dimension. For this reason the timings in 8 are not representative of the timings on real data where the entire volume is sampled.

**Influence of noise during training** Next, we study the influence of SNR on the reconstruction quality. We simulate the measurements with SNRs of  $-10$ dB,  $-5$ dB,  $0$ dB,  $5$ dB,  $10$ dB and also train the network with a range of noise levels, from  $-10$ dB to  $10$ dB. We test the models on the test volumes at different SNR levels. Figure 7 shows the SNR between the reference volume and the estimated volume. We can see that the network trained with a range of noise levels performs better than the network trained with a single noise level. Training CryoLithe on a range of different noise level makes it more robust to variation of noise level at test time. This comes at a cost of little or no loss in performance at a given, known noise level (which is anyway an unrealistic assumption).

**Influence of patch size** We evaluate the effect of varying the measurement neighborhood size while keeping the rest of the network architecture unchanged.<sup>5</sup> We expect larger neighborhoods to be beneficial for high-noise settings where additional context is valuable. To explore this we also vary noise level. Following the conclusions of the previous section, we train all the CryoLithe models on tilt-series with a range of noise in  $[-10, 10]$  dB.

Figure 8a shows the average reconstruction SNR at different noise levels. We observe that increasing the patch size improves the reconstruction SNR and that the gain is larger with stronger noise. However, patches larger than  $11 \times 11$  only marginally improve results. The main drawback of larger patches is the increased inference time; cf. Figure 8b. We evaluate the inference times of the 3D tomogram for different batch sizes, i.e., different numbers of voxels that are evaluated simultaneously. As expected, larger batch size always reduces the evaluation time, but at the cost of increasing the required memory. In practice one should choose the largest batch size that fits in the GPU memory. However, the size of the patch is highly dependent on the pixel size. In this experiment, the largest proteins are no larger than  $120\text{\AA}$ . With a patch of  $11 \times 11$  pixels, the maximum area captured from the projections is  $66^2$ , which is insufficient to fully capture the largest protein. To address this limitation, we selected patches of size  $21 \times 21$  pixels in experiments described above, ensuring that every protein could be fully captured within a single patch. For all batch sizes, the runtime scales with the patch size. Here again patches of size  $11 \times 11$  strike a balance between runtime and performance. If time is not a constraint, increasing the patch size can yield small improvements in quality.

<sup>5</sup>Or rather, almost unchanged: due to the larger input dimension the number of parameters in slice MLPs slightly increases with larger neighborhoods.

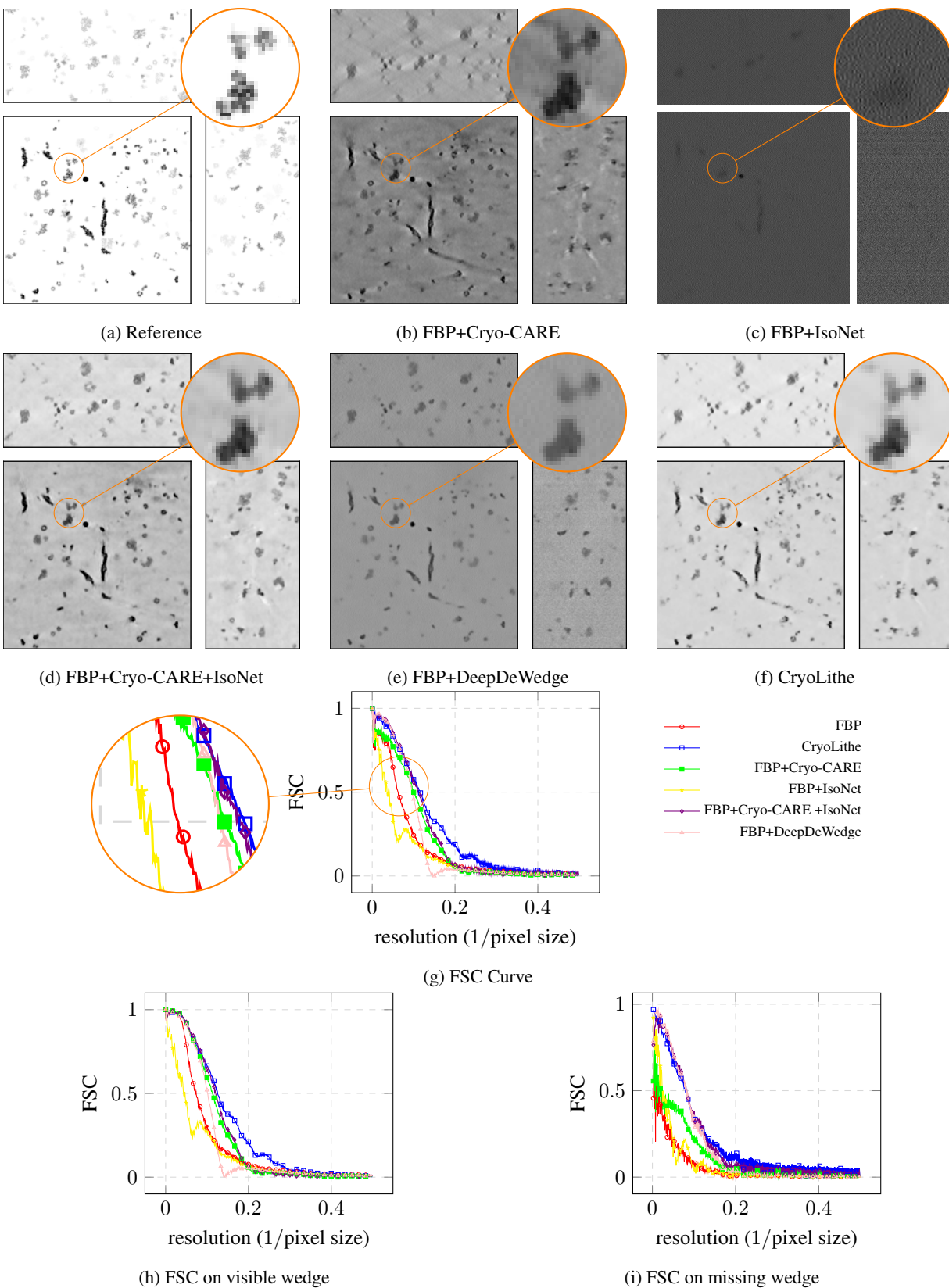


Figure 5: Evaluation of the reconstruction algorithms on simulated projections at SNR of -5dB. CryoLithe works on par with models that use large U-Nets. The FSC curves show that our model can recover part of the missing wedge even though it uses only local information, unlike some U-Net based architecture despite their large receptive field.

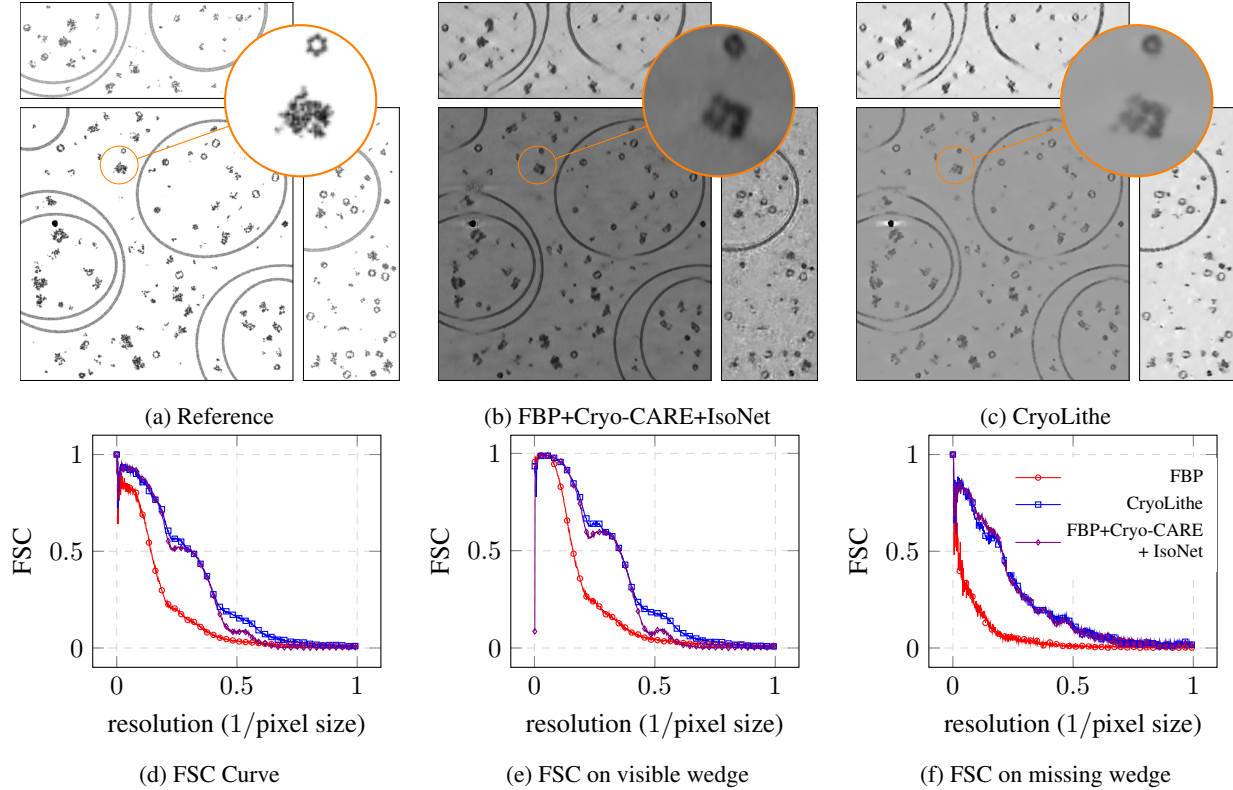


Figure 6: Evaluation of CryoLithe to reconstruct tilt-series from another collection of tomograms (model 0 from the SHREC dataset) different from the one used for training. The projections have SNR of -5dB. We compare against the best baseline, which was trained in a self-supervised manner specifically for the data of the figure. We see that CryoLithe successfully reconstructs tomograms that are different from the training data distribution.

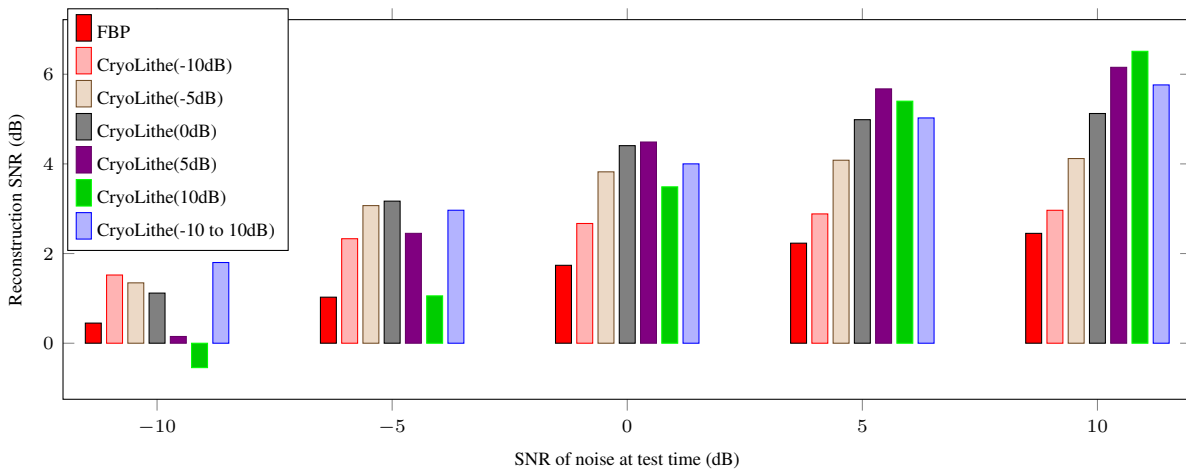


Figure 7: Influence of noise used to trained CryoLithe depending on the noise level observed at test time. Training on a well-chosen range of noise level, [-10dB, +10dB] in this experiment (rightmost bar), makes CryoLithe more robust to handle different noise levels at test time, while doing marginally worse than a network specifically trained for the same noise level as used at test time.

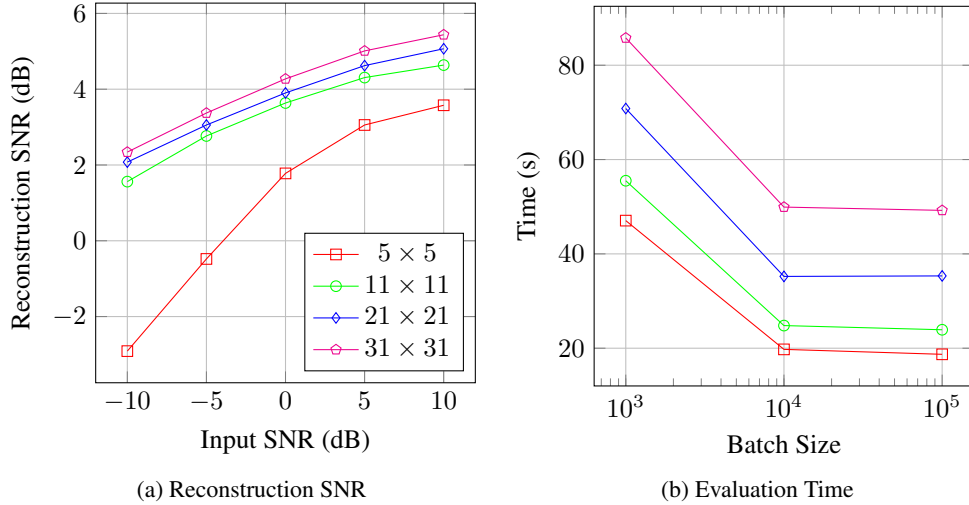


Figure 8: Evaluation of the effect of patch size of the models. The models are trained and tested using simulated data. The Reconstruction SNR plot shows reconstruction SNR with reference test volume for the trained models at different input SNR levels. Evaluation time plot shows the total evaluation time for the different models to recover the volumes.

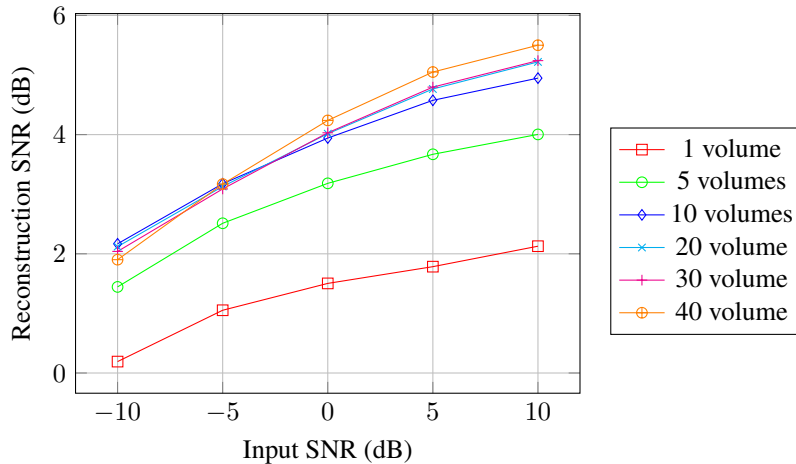


Figure 9: Influence of the number of training examples on the reconstruction SNR at different noise levels. As little as 10 volumes leads to almost best performance on the test dataset.

**Influence of training set size** A high-quality realistic training dataset is essential for the performance of CryoLithe. Here we explore the importance of the number of training volumes in reconstructing from cryo-TomoSim simulations. We trained networks with varying numbers of tomograms. All networks are trained on projections degraded by noise in the range  $[-10, 10]$ dB. Average reconstruction SNR on the test dataset is displayed in Figure 9 for different noise level.

We observe that at all noise levels, additional training volumes improve performances. Although we use realistic, diverse 3D volumes with more than 1000 different proteins, training on more than 10 volumes bring about only marginal benefits. We attribute this to the robustness of CryoLithe to distribution shifts due to locality, which prevents over-fitting.

#### 4.1.3 Reconstruction with real tilt-series

We test CryoLithe on different real tilt-series, *while training exclusively on simulated data* as elaborated above. In Section 4.2 we show that these results can be further improved and made more robust by using a carefully designed training set from real tilt-series.

We first consider the widely used EMPIAR-10045 dataset, which contains 7 tilt-series of purified *S. cerevisiae* 80S Ribosomes. Note that the dataset is similar to the training set, where the proteins are placed randomly at empty spaces, with empty spaces representing the solution in which the proteins are floating. The tilt-series contains 41 aligned

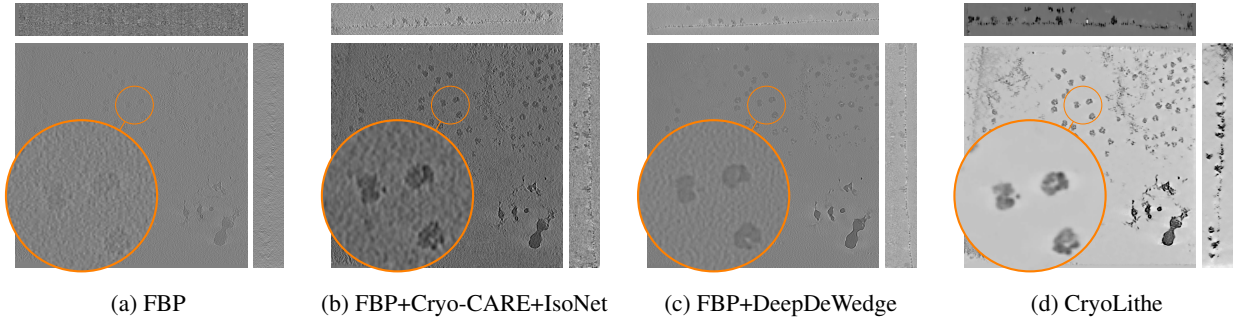


Figure 10: CryoLithe, trained on synthetic data composed of isolated proteins, accurately reconstruct similar real tilt-series composed of 80S ribosome (EMPIAR-10045).

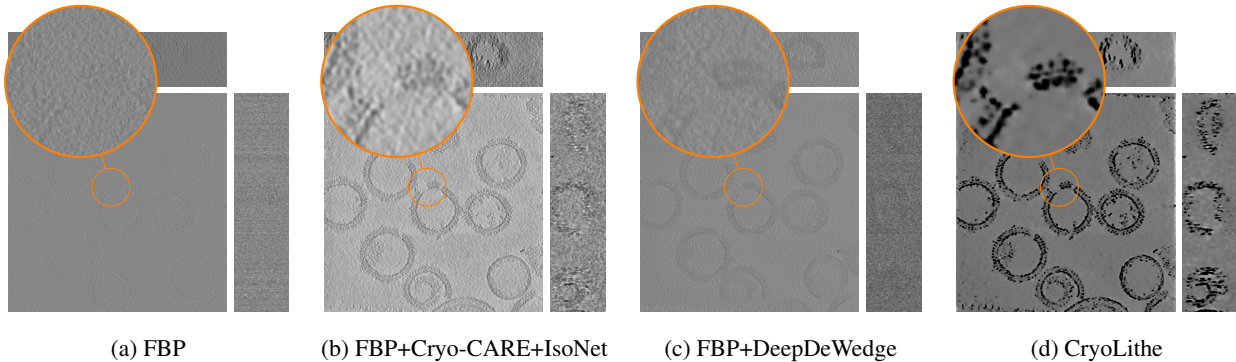


Figure 11: CryoLithe, trained on synthetic data composed of isolated proteins, accurately reconstruct different real tilt-series composed of HIV-1 Gag protein assemblies (EMPIAR-10643).

projections between  $-60$  to  $60$  degrees sampled at  $2.17\text{\AA}/\text{px}$ . We apply the different reconstructions approaches on the tilt-series from 'tomogram 5' after downsampling it by a factor of 4. Results are shown in Figure 10. First, we observe that CryoLithe trained on simulated data reconstructs empty space significantly smoother than other methods, which indicates better denoising performance. Second, particles are retrieved with much more precision. For instance, we can directly distinguish the large and small ribosomal subunits with a cavity in between as shown in Figure 10d. The best baseline in this example, DeepDeWedge, does not reach this level of detail. Note that we downsample projections by a factor of 4 as this is the smallest downsampling rate that allows the baseline to fit in memory. This way the evaluation is uniform across different volumes. A different resampling may either improve or worsen results as it affects the signal-to-noise ratio of the resulting tilt series and the number of observed cells and proteins.

Next, we consider the EMPIAR-10643 dataset, comprising 5 tilt-series of isolated HIV-1 Gag protein assemblies, each with 41 projections between  $-60$  and  $60$  degrees. Projections are of size  $4096 \times 4096$  sampled at  $1.179\text{\AA}/\text{px}$ . Since the tilt-series is unaligned we first use IMODs fiducial alignment tool (this sample contains fiducial markers). We evaluate CryoLithe on such a dataset. As shown in Figure 11 (tilt-series 'b2tilt40.mrc' downsampled by a factor of 4), this dataset contains distinct spherical assemblies with embedded Gag proteins. While still being a dataset of isolated proteins, it is an excellent test case for CryoLithe as it is significantly different from training data which contains smaller proteins in empty space. A visual comparison of the reconstructions in Figure 11 reveals that CryoLithe outperforms state-of-the-art reconstruction methods on EMPIAR-10643. Notably, it accurately reconstructs HIV-1 protein structures not seen during training. This robustness is important. It highlights CryoLithe's ability to decode arbitrary structures which will be essential in exploratory cellular imaging.

#### 4.2 Training with pairs of real tilt-series and tomograms

While training CryoLithe on synthetic data allows us to accurately reconstruct simple tomograms, it does not perform as well for crowded volumes with arbitrary cellular structures, ice artifacts, and other features that are challenging to simulate. To overcome these problems, we constructed a training dataset from real tilt-series. The associated target volumes were reconstructed using a combination of FBP, Cryo-CARE and IsoNet on the aligned tilt-series.

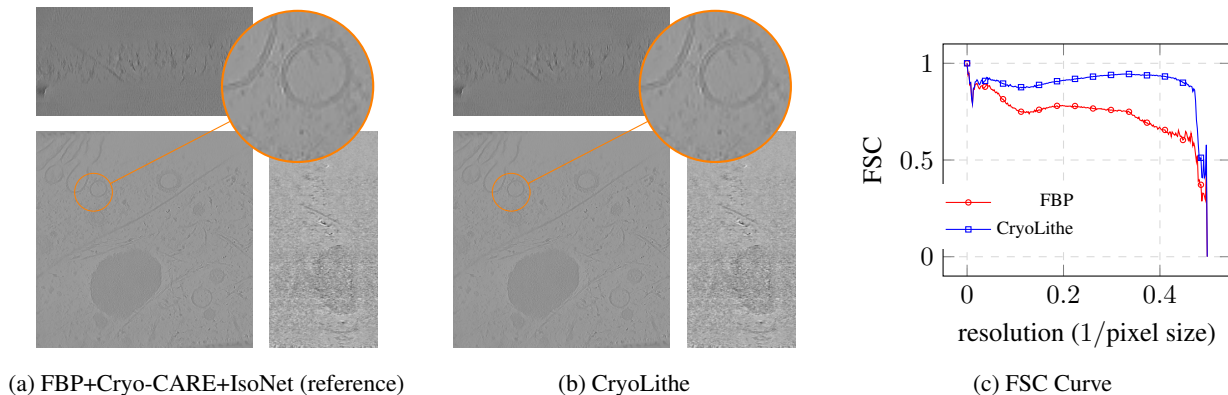


Figure 12: Evaluation of CryoLithe trained on the real dataset. The FSC curves are computed using the volume recovered from FBP+Cryo-CARE + IsoNet as reference. The FSC curve is close to 1 for most frequencies, which indicates that the model can closely recover the reference reconstruction.

We selected tilt-series from the EMPIAR-11830 dataset [68] which contains *Chlamydomonas reinhardtii* samples prepared using cryo-plasma FIB milling. The dataset comprises 1829 tilt-series, with the number of projections per series ranging between 16 and 61. This variation arises because some projections were removed due to measurement artifacts such as large ice obstructions or too much drift. The projections are of size  $4096 \times 4096$  sampled at  $1.96\text{\AA}/\text{pixel}$ .

The dataset contains tilt-series pairs generated by an even-odd split of the raw frames. Tilt-series were aligned using AreTomo on the "full" (all frames) stack, which is then used to reconstruct tomogram pairs from the even-odd split. The even-odd reconstructions are therefore identical except for the noise. It also contains Cryo-CARE reconstructions using  $4\times$  downsampled projections. To prepare a training set for CryoLithe, we first selected all tilt-series with exactly 41 projections. We focus on 41 projections for simplicity and we plan to release a model that is agnostic to the number of projections in the future. We then visually inspected all corresponding Cryo-CARE and FBP reconstructions and carefully ranked the large remaining number of Cryo-CARE reconstructions based on the presence of artifacts and quality of denoising, retaining the top 20. We downsampled the projections by a factor of 4 to match the reference reconstructed volumes, resulting in a sampling rate of  $7.84\text{\AA}/\text{pixels}$ . As the last step, we further refined the volumes using IsoNet, which helped mitigate missing wedge artifacts and improve denoising. As some IsoNet reconstructions showed artifacts we conducted additional visual inspections and excluded any tilt-series with artifact-laden reconstructions. Ultimately, we kept 13 pairs of tilt-series and corresponding FBP+Cryo-CARE+IsoNet reconstructions: 10 for training, 2 for validation and 1 for testing.

#### 4.2.1 Reconstruction of simple tilt-series

We use the same network architecture and same training procedure as described in Section 4.1 but using our curated real paired data for training. We first evaluate the reconstruction quality on the test volume. Figure 12 shows that CryoLithe reconstruction is similar to the reference tomogram given by FBP+Cryo-CARE+IsoNet. This is corroborated by the FSC curve that stays close to 1 throughout the frequency range. We emphasize that even this test volume differs substantially in content and thus distribution from the training dataset which comprises only 7 (albeit high-quality) examples.

We now further investigate the robustness to distribution shifts. To this end, we use CryoLithe to reconstruct EMPIAR-10045 which contains isolated ribosomes (Figure 13), and EMPIAR-10643 which contains HIV-1 Gag protein assemblies (Figure 14). We see that CryoLithe recovers the Gag protein details in the HIV dataset better than the self-supervised methods. CryoLithe is again able to properly reconstruct tilt-series not seen during training, while requiring low GPU memory and significantly less time than self-supervised baselines (see Table 1).

#### 4.2.2 Testing on a real tilt-series from a different sample

Training CryoLithe on real rather than purely synthetic data becomes essential when processing complex, crowded cellular volumes with high amount of noise and possibly ice artifacts. We illustrate this on the 'tomo6' tilt-series from EMPIAR-12262 [69] which contains non-infected cos-7 cells sampled at  $5.525\text{\AA}/\text{pixel}$ . We downsample the projection by a factor of 3. The tilt-series is acquired between  $-51$  and  $51$  degrees, with projections of size  $1279 \times 1236$ . We use AreTomo to align the projections prior to reconstruction.

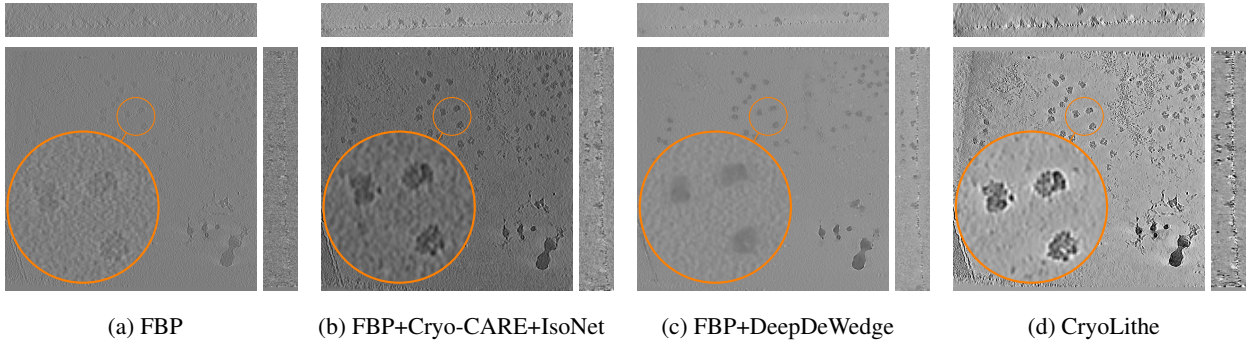


Figure 13: Evaluation of CryoLiteh, trained on the real dataset, on EMPIAR-10045 (isolated ribosome proteins).

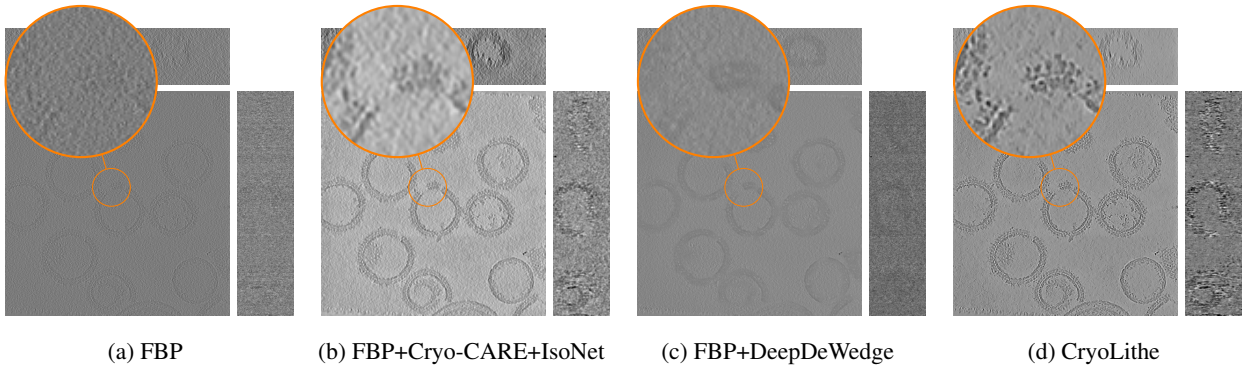


Figure 14: Evaluation of CryoLiteh, trained on the real dataset, on EMPIAR-10643 (HIV complexes). The spikes are better visible in CryoLiteh’s reconstruction compared to others.

We emphasize the many experimental differences between this tilt-series and those used for training: first and foremost, the biological sample is very different. Also, it was acquired at a different microscope. Furthermore, there is a considerable mismatch in the tilt range, tilt step (2.5 vs. 2.0 degrees), projection size and sampling rate between the training data and this tilt-series, although the number of projections is the same (41).

We showcase CryoLiteh’s reconstruction alongside FBP and FBP+Cryo-CARE+IsoNet reconstructions in Figure 15. Visually, the reconstruction is close to FBP+Cryo-CARE+IsoNet. The advantage of CryoLiteh is that it computes the reconstruction 7 times faster and does not require any hyperparameter tuning that might be challenging for non-experts. We further observe that the empty regions in the reconstruction are better denoised (“flattened”) compared to FBP+Cryo-CARE+IsoNet. Furthermore, CryoLiteh performs well despite all the differences between the training and the test data outlined above, again showing its robustness to distribution shifts.

### 4.3 Improve denoising

Modern direct detectors collect multiple frames at each tilt angle, allowing compensation of beam-induced motion [70]. By aligning and averaging these frames, we obtain sharper images. Self-supervised denoising frameworks such as Cryo-CARE and Topaz-Denoise group the frames into two subsets to generate independent noisy realizations of the measurements, enabling training in a Noise2Noise framework.

CryoLiteh can benefit from the Noise2Noise framework when multiple independent and identically distributed tilt-series are available. In our approach, we use only a single realization of the measurements to train the network. However, we leverage the availability of independent realizations as a data augmentation strategy. Specifically, we experiment with two data augmentation techniques: ‘Odd/Even’, using both realizations of the measurements as separate inputs (with the same target tomogram) and ‘Swapped’, swapping randomly projections between the two realizations to create additional data points. We applied these strategies and compared the network’s performance on the ribosome dataset.

Figure 16 shows the effect of these data augmentation techniques on reconstruction quality compared to using standard averaged projections, referred as ‘Averaged’. ‘Odd/Even’ refers to randomly selecting one realization for each epoch, and ‘Swapped’ indicates that some projections are randomly exchanged between the two tilt-series. We observe that the

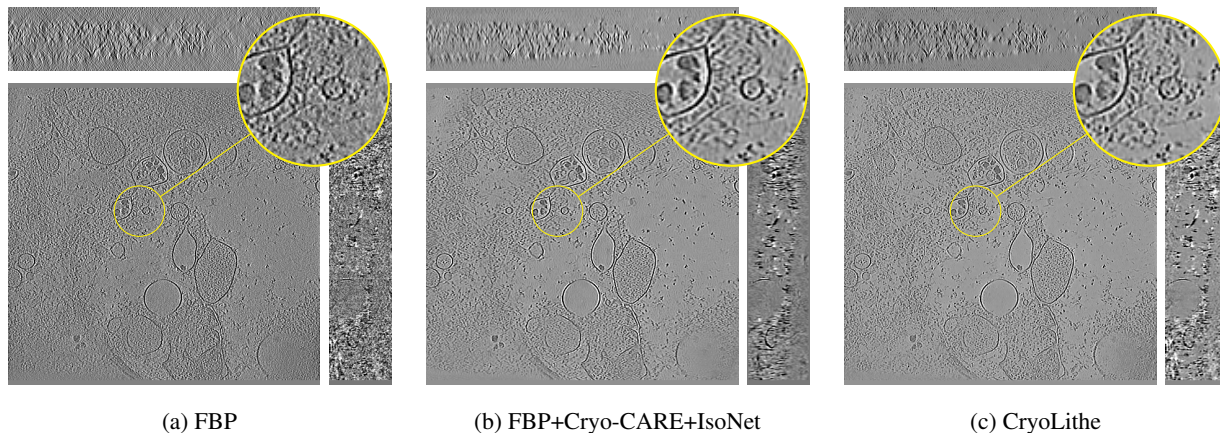


Figure 15: Evaluation of CryoLithe on a tilt-series from EMPIAR-12262. Tilt-series represents a different biological sample, and contains different measurement range, sampling rate and projection size than the training dataset, and it comes from a different microscope. Despite these challenges, CryoLithe reconstruction is similar to that of FBP+Cryo-CARE+IsoNet, but with faster inference and no hyperparameter to tune.

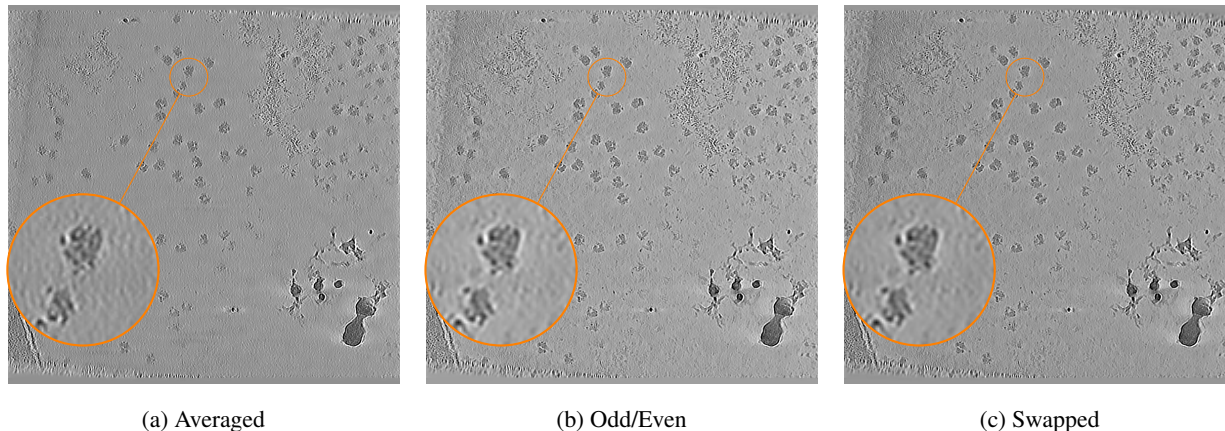


Figure 16: Evaluation of data augmentation strategies to improve denoising. Input odd/even tilt-series are either fully averaged (a), randomly chosen (b) or some projections are randomly swapped (c). Both data augmentation (b) and (c) techniques improve the denoising capacity of CryoLithe.

network trained with the proposed data augmentation steps performs better visually, compared to network trained with fully averaged projections. This can be seen with the increase in contrast between the empty regions and the region with particle, as well as a clear differentiation between the background and the particles in the figure.

## 5 Discussion and outlook

The availability of cryo-ET datasets is growing fast; as a case in point, EMPIAR-11830 alone has almost 2,000 volumes [68]. This expansion will likely accelerate as more laboratories around the world bring the latest generation of electron microscopes online and train new users, coupled with advances in sample preparation and automation of microscopy sessions. There is thus a growing need for fast, reliable reconstruction methods.

CryoLithe can be used off-the-shelf to efficiently reconstruct arbitrary volumes. Training on new data is also straightforward—though, as shown here, hardly necessary—making it easy for both experienced users and novices to obtain high-quality reconstructions in a short time compared with self-supervised methods. In principle, self-supervised approaches could also be accelerated by training on a larger dataset; DeepDeWedge suggests using up to ten similar volumes (e.g., from the same cell type). However, extending self-supervised strategies to much larger datasets is generally challenging and the issues of robustness to distribution shift remain. By contrast, CryoLithe is specifically designed to be robust to such variations.



A particularly time-consuming aspect of developing CryoLithe was the painstaking manual curation of a high-quality training set from EMPIAR, which required repeatedly running existing self-supervised reconstruction methods, and visually inspecting the tomograms slice by slice. We believe this curated dataset will be valuable for others developing deep-learning-based approaches and anticipate the need for a more scalable curation strategy as we work to further improve results. Such data are also useful for building deep learning methods in other stages of the cryo-ET pipeline, including denoising, missing wedge compensation, tilt-series alignment, and incorporating diffraction effects.

As resolution continues to improve, refinements to the forward model (1) may become necessary—for instance, to account for diffraction effects (especially relevant in thick samples or lower electron energies [71]) and to handle the contrast transfer function (CTF) more explicitly. The global filtering + nonlinear local “backprojection” framework implemented in CryoLithe can be adapted to handle these more complex physics. For the current state of cryo-ET, where resolutions typically remain around 8–10 Å, the forward model in (1) is standard and effective.

Our approach achieves results comparable to or better than the current state-of-the-art methods. Its advantages include ease of use with no need for parameter tuning, low resource requirements and robustness to unseen data without introducing hallucinated artifacts. Our best-trained model is available by downloading the network weights and running a Python script. A next step is to integrate CryoLithe into Scipion [72], which unifies multiple cryo-EM/ET image-processing packages under one interface. This would make CryoLithe accessible to an even broader user base.

We emphasize that CryoLithe is a live project, and we aim to improve the codebase, interface, and overall performance continuously. A major advantage of our approach is that it is a new paradigm with ample headroom, while even our initial implementation already delivers excellent reconstructions at high speed. Finally, the design philosophy behind CryoLithe—combining learned global filtering with local nonlinear inference—can be applied to other challenging 3D imaging problems beyond cryo-ET.

## References

- [1] P. P. Navarro, “Quantitative cryo-electron tomography,” *Frontiers in Molecular Biosciences*, vol. 9, p. 934465, 2022.
- [2] D. Cressley and E. Callaway, “Cryo-electron microscopy wins chemistry nobel,” *Nature*, vol. 550, no. 7675, 2017.
- [3] A. Faruqi and R. Henderson, “Electronic detectors for electron microscopy,” *Current opinion in structural biology*, vol. 17, no. 5, pp. 549–555, 2007.
- [4] P. T. Kim, A. J. Noble, A. Cheng, and T. Bepler, “Learning to automate cryo-electron microscopy data collection with Ptolemy,” *arXiv:2112.01534 [cs, eess, q-bio]*, Dec. 2021. arXiv: 2112.01534.
- [5] K. Maruthi, M. Kopylov, and B. Carragher, “Automating decision making in the cryo-em pre-processing pipeline,” *Structure*, vol. 28, no. 7, pp. 727–729, 2020.
- [6] T. Nakane, A. Kotecha, A. Sente, G. McMullan, S. Masiulis, P. M. G. E. Brown, I. T. Grigoras, L. Malinauskaite, T. Malinauskas, J. Miehling, T. Uchański, L. Yu, D. Karia, E. V. Pechnikova, E. D. Jong, J. Keizer, M. Bischoff, J. McCormack, P. Tiemeijer, and S. H. W. Scheres, “Single-particle cryo-EM at atomic resolution,” *Nature*, no. May, 2020.
- [7] K. M. Yip, N. Fischer, E. Paknia, A. Chari, and H. Stark, “Atomic-resolution protein structure determination by cryo-em,” *Nature*, vol. 587, no. 7832, pp. 157–161, 2020.
- [8] K. Zhang, G. D. Pintilie, S. Li, M. F. Schmid, and W. Chiu, “Resolving individual atoms of protein complex by cryo-electron microscopy,” *Cell research*, vol. 30, no. 12, pp. 1136–1139, 2020.
- [9] A. C. Kak and M. Slaney, *Principles of computerized tomographic imaging*. SIAM, 2001.
- [10] G. Harauz and M. van Heel, “Exact filters for general geometry three dimensional reconstruction.,” *Optik.*, vol. 73, no. 4, pp. 146–156, 1986.
- [11] T.-O. Buchholz, M. Jordan, G. Pigino, and F. Jug, “Cryo-care: Content-aware image restoration for cryo-transmission electron microscopy data,” in *2019 IEEE 16th International Symposium on Biomedical Imaging (ISBI 2019)*, pp. 502–506, IEEE, 2019.
- [12] J. Lehtinen, J. Munkberg, J. Hasselgren, S. Laine, T. Karras, M. Aittala, and T. Aila, “Noise2noise: Learning image restoration without clean data,” *arXiv preprint arXiv:1803.04189*, 2018.
- [13] T. Bepler, K. Kelley, A. J. Noble, and B. Berger, “Topaz-denoise: general deep denoising models for cryoem and cryoet,” *Nature communications*, vol. 11, no. 1, p. 5208, 2020.
- [14] Y. Shkolnisky and A. Singer, “Viewing direction estimation in cryo-em using synchronization,” *SIAM journal on imaging sciences*, vol. 5, no. 3, pp. 1088–1110, 2012.

- [15] Y.-T. Liu, H. Zhang, H. Wang, C.-L. Tao, G.-Q. Bi, and Z. H. Zhou, "Isotropic reconstruction for electron tomography with deep learning," *Nature communications*, vol. 13, no. 1, p. 6482, 2022.
- [16] S. Wiedemann and R. Heckel, "A deep learning method for simultaneous denoising and missing wedge reconstruction in cryogenic electron tomography," *Nature Communications*, vol. 15, no. 1, p. 8255, 2024.
- [17] E. T. Quinto, U. Skoglund, and O. Öktem, "Electron lambda-tomography," *Proceedings of the National Academy of Sciences*, vol. 106, no. 51, pp. 21842–21847, 2009.
- [18] S. K. Burley, H. M. Berman, G. J. Kleywegt, J. L. Markley, H. Nakamura, and S. Velankar, "Protein data bank (pdb): the single global macromolecular structure archive," *Protein crystallography: methods and protocols*, pp. 627–641, 2017.
- [19] A. Martinez-Sanchez, L. Lamm, M. Jasnin, and H. Phelippeau, "Simulating the cellular context in synthetic datasets for cryo-electron tomography," *bioRxiv*, pp. 2023–05, 2023.
- [20] L. Lamm, S. Zufferey, R. D. Righetto, W. Wietrzynski, K. A. Yamauchi, A. Burt, Y. Liu, H. Zhang, A. Martinez-Sanchez, S. Ziegler, *et al.*, "Membrain v2: an end-to-end tool for the analysis of membranes in cryo-electron tomography," *bioRxiv*, pp. 2024–01, 2024.
- [21] M. Harastani, G. Patra, C. Kervrann, and M. Eltsov, "Template learning: Deep learning with domain randomization for particle picking in cryo-electron tomography," *bioRxiv*, pp. 2024–03, 2024.
- [22] C. Purnell, J. Heebner, M. T. Swulius, R. Hylton, S. Kabonick, M. Grillo, S. Grigoryev, F. Heberle, M. N. Waxham, and M. T. Swulius, "Rapid synthesis of cryo-et data for training deep learning models," *bioRxiv*, 2023.
- [23] A. Khorashadizadeh, V. Debarnot, T. Liu, and I. Dokmanić, "Glimpse: Generalized local imaging with mlps," *arXiv preprint arXiv:2401.00816*, 2024.
- [24] M. Adrian, J. Dubochet, J. Lepault, and A. W. McDowell, "Cryo-electron microscopy of viruses," *Nature*, vol. 308, pp. 32–36, Mar. 1984. ISBN: 0028-0836 (Print).
- [25] R. I. Koning, A. J. Koster, and T. H. Sharp, "Advances in cryo-electron tomography for biology and medicine," *Annals of Anatomy-Anatomischer Anzeiger*, vol. 217, pp. 82–96, 2018.
- [26] X. Li, P. Mooney, S. Zheng, C. R. Booth, M. B. Braunfeld, S. Gubbens, D. A. Agard, and Y. Cheng, "Electron counting and beam-induced motion correction enable near-atomic-resolution single-particle cryo-em," *Nature methods*, vol. 10, no. 6, pp. 584–590, 2013.
- [27] R. M. Glaeser, "Limitations to significant information in biological electron microscopy as a result of radiation damage," *Journal of ultrastructure research*, vol. 36, no. 3-4, pp. 466–482, 1971.
- [28] R. Henderson, "The potential and limitations of neutrons, electrons and X-rays for atomic resolution microscopy of unstained biological molecules," *Quarterly Reviews of Biophysics*, vol. 28, no. 02, pp. 171–193, 1995.
- [29] S. Q. Zheng, E. Palovcak, J.-P. Armache, K. A. Verba, Y. Cheng, and D. A. Agard, "MotionCor2: anisotropic correction of beam-induced motion for improved cryo-electron microscopy," *Nature Methods*, vol. 14, pp. 331–332, Apr. 2017. Publisher: Nature Publishing Group, a division of Macmillan Publishers Limited. All Rights Reserved.
- [30] T. Grant and N. Grigorieff, "Measuring the optimal exposure for single particle cryo-EM using a 2.6 Å reconstruction of rotavirus VP6," *eLife*, vol. 4, May 2015.
- [31] A. Rohou and N. Grigorieff, "Ctffind4: Fast and accurate defocus estimation from electron micrographs," *Journal of structural biology*, vol. 192, no. 2, pp. 216–221, 2015.
- [32] D. N. Mastronarde and S. R. Held, "Automated tilt series alignment and tomographic reconstruction in IMOD," *Journal of Structural Biology*, vol. 197, pp. 102–113, Feb. 2017. Publisher: Elsevier Inc. ISBN: 1047-8477.
- [33] S. Zheng, G. Wolff, G. Greenan, Z. Chen, F. G. Faas, M. Bárcena, A. J. Koster, Y. Cheng, and D. A. Agard, "Aretomo: An integrated software package for automated marker-free, motion-corrected cryo-electron tomographic alignment and reconstruction," *Journal of Structural Biology: X*, vol. 6, p. 100068, 2022.
- [34] V. Debarnot, V. Kishore, R. D. Righetto, and I. Dokmanić, "Ice-tide: Implicit cryo-et imaging and deformation estimation," *arXiv preprint arXiv:2403.02182*, 2024.
- [35] A. H. Andersen and A. C. Kak, "Simultaneous algebraic reconstruction technique (sart): a superior implementation of the art algorithm," *Ultrasonic imaging*, vol. 6, no. 1, pp. 81–94, 1984.
- [36] P. Gilbert, "Iterative methods for the three-dimensional reconstruction of an object from projections," *Journal of theoretical biology*, vol. 36, no. 1, pp. 105–117, 1972.
- [37] L. A. Feldkamp, L. C. Davis, and J. W. Kress, "Practical cone-beam algorithm," *Josa a*, vol. 1, no. 6, pp. 612–619, 1984.

- [38] A. Stoschek and R. Hegerl, “Denoising of electron tomographic reconstructions using multiscale transformations,” *Journal of structural biology*, vol. 120, no. 3, pp. 257–265, 1997.
- [39] R. S. Pantelic, R. Rothnagel, C.-Y. Huang, D. Muller, D. Woolford, M. J. Landsberg, A. McDowall, B. Pailthorpe, P. R. Young, J. Banks, *et al.*, “The discriminative bilateral filter: an enhanced denoising filter for electron microscopy data,” *Journal of structural biology*, vol. 155, no. 3, pp. 395–408, 2006.
- [40] P. van der Heide, X.-P. Xu, B. J. Marsh, D. Hanein, and N. Volkman, “Efficient automatic noise reduction of electron tomographic reconstructions based on iterative median filtering,” *Journal of structural biology*, vol. 158, no. 2, pp. 196–204, 2007.
- [41] A. S. Frangakis and R. Hegerl, “Noise reduction in electron tomographic reconstructions using nonlinear anisotropic diffusion,” *Journal of structural biology*, vol. 135, no. 3, pp. 239–250, 2001.
- [42] B. Mildenhall, P. P. Srinivasan, M. Tancik, J. T. Barron, R. Ramamoorthi, and R. Ng, “Nerf: Representing scenes as neural radiance fields for view synthesis,” *Communications of the ACM*, vol. 65, no. 1, pp. 99–106, 2021.
- [43] V. Sitzmann, J. Martel, A. Bergman, D. Lindell, and G. Wetzstein, “Implicit neural representations with periodic activation functions,” *Advances in neural information processing systems*, vol. 33, pp. 7462–7473, 2020.
- [44] Y. Wang, R. Idoughi, and W. Heidrich, “Learning adaptive tensorial density fields for clean cryo-et reconstruction,” *Advances in Neural Information Processing Systems*, vol. 36, 2024.
- [45] Y. Wang, R. Idoughi, D. Rückert, R. Li, and W. Heidrich, “Adaptive differentiable grids for cryo-electron tomography reconstruction and denoising,” *Bioinformatics Advances*, vol. 3, no. 1, p. vbad131, 2023.
- [46] J. M. Parkhurst, M. Dumoux, M. Basham, D. Clare, C. A. Siebert, T. Varslot, A. Kirkland, J. H. Naismith, and G. Evans, “Parakeet: a digital twin software pipeline to assess the impact of experimental parameters on tomographic reconstructions for cryo-electron tomography,” *Open Biology*, vol. 11, no. 10, p. 210160, 2021.
- [47] M. Vulović, R. B. Ravelli, L. J. van Vliet, A. J. Koster, I. Lazić, U. Lücken, H. Rullgård, O. Öktem, and B. Rieger, “Image formation modeling in cryo-electron microscopy,” *Journal of structural biology*, vol. 183, no. 1, pp. 19–32, 2013.
- [48] P. Harar, L. Herrmann, P. Grohs, and D. Haselbach, “Faket: Simulating cryo-electron tomograms with neural style transfer,” *arXiv preprint arXiv:2304.02011*, 2023.
- [49] H. Rullgård, L.-G. Öfverstedt, S. Masich, B. Daneholt, and O. Öktem, “Simulation of transmission electron microscope images of biological specimens,” *Journal of microscopy*, vol. 243, no. 3, pp. 234–256, 2011.
- [50] B. Himes and N. Grigorieff, “Cryo-tem simulations of amorphous radiation-sensitive samples using multislice wave propagation,” *IUCrJ*, vol. 8, no. 6, pp. 943–953, 2021.
- [51] T. Würfl, M. Hoffmann, V. Christlein, K. Breininger, Y. Huang, M. Unberath, and A. K. Maier, “Deep learning computed tomography: Learning projection-domain weights from image domain in limited angle problems,” *IEEE transactions on medical imaging*, vol. 37, no. 6, pp. 1454–1463, 2018.
- [52] Y. Li, K. Li, C. Zhang, J. Montoya, and G.-H. Chen, “Learning to reconstruct computed tomography images directly from sinogram data under a variety of data acquisition conditions,” *IEEE transactions on medical imaging*, vol. 38, no. 10, pp. 2469–2481, 2019.
- [53] J. He, Y. Wang, and J. Ma, “Radon inversion via deep learning,” *IEEE transactions on medical imaging*, vol. 39, no. 6, pp. 2076–2087, 2020.
- [54] B. Hamoud, Y. Bahat, and T. Michaeli, “Beyond local processing: Adapting cnns for ct reconstruction,” in *European Conference on Computer Vision*, pp. 513–526, Springer, 2022.
- [55] A. Khorashadizadeh, A. Chaman, V. Debarnot, and I. Dokmanić, “Funknn: Neural interpolation for functional generation,” in *The Eleventh International Conference on Learning Representations*, 2022.
- [56] A. Khorashadizadeh, T. I. Liaudat, T. Liu, J. D. McEwen, and I. Dokmanić, “Lofi: Neural local fields for scalable image reconstruction,” *arXiv preprint arXiv:2411.04995*, 2024.
- [57] I. O. Tolstikhin, N. Houlsby, A. Kolesnikov, L. Beyer, X. Zhai, T. Unterthiner, J. Yung, A. Steiner, D. Keysers, J. Uszkoreit, *et al.*, “Mlp-mixer: An all-mlp architecture for vision,” *Advances in neural information processing systems*, vol. 34, pp. 24261–24272, 2021.
- [58] Y. Mansour, K. Lin, and R. Heckel, “Image-to-image mlp-mixer for image reconstruction,” *arXiv preprint arXiv:2202.02018*, 2022.
- [59] B. Turoňová, F. K. Schur, W. Wan, and J. A. Briggs, “Efficient 3d-ctf correction for cryo-electron tomography using novactf improves subtomogram averaging resolution to 3.4 Å,” *Journal of structural biology*, vol. 199, no. 3, pp. 187–195, 2017.

- [60] D. N. Mastronarde, “Accurate, automatic determination of astigmatism and phase with Ctfplotter in IMOD,” *Journal of Structural Biology*, vol. 216, p. 108057, Mar. 2024.
- [61] M. Vulović, L. M. Voortman, L. J. van Vliet, and B. Rieger, “When to use the projection assumption and the weak-phase object approximation in phase contrast cryo-em,” *Ultramicroscopy*, vol. 136, pp. 61–66, 2014.
- [62] D. P. Kingma, “Adam: A method for stochastic optimization,” *arXiv preprint arXiv:1412.6980*, 2014.
- [63] S. Mohan, Z. Kadkhodaie, E. P. Simoncelli, and C. Fernandez-Granda, “Robust and interpretable blind image denoising via bias-free convolutional neural networks,” *arXiv preprint arXiv:1906.05478*, 2019.
- [64] A. A. Hendriksen, D. Schut, W. J. Palenstijn, N. Viganó, J. Kim, D. M. Pelt, T. Van Leeuwen, and K. J. Batenburg, “Tomosipo: fast, flexible, and convenient 3d tomography for complex scanning geometries in python,” *Optics Express*, vol. 29, no. 24, pp. 40494–40513, 2021.
- [65] P. D. Bank, “Protein data bank,” *Nature New Biol*, vol. 233, no. 223, pp. 10–1038, 1971.
- [66] G. Harauz and M. van Heel, “Exact filters for general geometry three dimensional reconstruction,” *Optik*, vol. 78, no. 4, pp. 146–156, 1986. ISBN: 0030-4026.
- [67] I. Gubins, M. L. Chaillet, G. van Der Schot, R. C. Veltkamp, F. Förster, Y. Hao, X. Wan, X. Cui, F. Zhang, E. Moebel, *et al.*, “Shrec 2020: Classification in cryo-electron tomograms,” *Computers & Graphics*, vol. 91, pp. 279–289, 2020.
- [68] R. Kelley, S. Khavnekar, R. D. Righetto, J. Heebner, M. Obr, X. Zhang, S. Chakraborty, G. Tagiltsev, A. K. Michael, S. v. Dorst, F. Waltz, C. L. McCafferty, L. Lamm, S. Zufferey, P. V. d. Stappen, H. v. d. Hoek, W. Wietrzynski, P. Harar, W. Wan, J. A. G. Briggs, J. M. Plitzko, B. D. Engel, and A. Kotecha, “Towards community-driven visual proteomics with large-scale cryo-electron tomography of *Chlamydomonas reinhardtii*,” Dec. 2024. Pages: 2024.12.28.630444 Section: New Results.
- [69] A. Ishemgulova, L. Mukhamedova, Z. Trebichalská, V. Rájecká, P. Payne, L. Šmerdová, J. Moravcová, D. Hřebík, D. Buchta, K. Škubník, *et al.*, “Endosome rupture enables enteroviruses from the family picornaviridae to infect cells,” *Communications Biology*, vol. 7, no. 1, p. 1465, 2024.
- [70] A. F. Brilot, J. Z. Chen, A. Cheng, J. Pan, S. C. Harrison, C. S. Potter, B. Carragher, R. Henderson, and N. Grigorieff, “Beam-induced motion of vitrified specimen on holey carbon film,” *Journal of Structural Biology*, vol. 177, pp. 630–637, Mar. 2012.
- [71] C. J. Russo, J. L. Dickerson, and K. Naydenova, “Cryomicroscopy in situ: what is the smallest molecule that can be directly identified without labels in a cell?,” *Faraday Discussions*, Aug. 2022. Publisher: The Royal Society of Chemistry.
- [72] P. Conesa, Y. C. Fonseca, J. J. de la Morena, G. Sharov, J. M. de la Rosa-Trevín, A. Cuervo, A. G. Mena, B. R. de Francisco, D. Del Hoyo, D. Herreros, *et al.*, “Scipion3: A workflow engine for cryo-electron microscopy image processing and structural biology,” *Biological Imaging*, vol. 3, p. e13, 2023.

## A Experimental parameters

All initial FBP reconstructions were obtained using IMOD with supersampling enabled. This approach was chosen to mitigate aliasing artifacts often observed in FBP reconstructions for limited measurements. Two FBP reconstructions were generated with two different noisy sets of projections of the same volume. The baseline methods were then evaluated using the following configurations. Run-time summary is available in Table 1. The parameters used are as follows:

1. FBP+Cryo-CARE: we crop 1,200 subtomograms of size  $72 \times 72 \times 72$  from the two FBP tomograms. For training the Cryo-CARE model, we use a U-Net with a depth of 3, a filter size of 3, and 16 channels in the first layer. The model is trained for 100 epochs, with 200 steps per epoch.
2. FBP+IsoNet: we average reconstructions from the two noisy measurements and crop 100 subtomograms of size  $80 \times 80 \times 80$ . IsoNet employs a fixed U-Net architecture, so the default network parameters are used. The network is trained for 30 iterations, with artificial noise of increasing variance added to the subtomograms during iterations 10, 15, 20, and 25.
3. FBP+Cryo-CARE+IsoNet: Cryo-CARE is trained as described in FBP + Cryo-CARE configuration. Similarly, IsoNet is trained following the settings described in FBP + IsoNet. The only difference being that the output from Cryo-CARE is used as input for training IsoNet.

4. FBP+deepDeWedge: subtomograms of size  $96 \times 96 \times 96$  is used for this method. A U-Net with 3 layers and 32 input channels is trained for 1000 epochs. However, due to memory constraints during the timing experiment, the network was run for 750 epochs.

While evaluating the baseline methods, we followed the default parameter configuration suggested by the authors. For experiments with real datasets, such as the HIV-1 and ribosome 80S datasets, dose-fractionated data was not available. In these cases, we generated two measurement sets by dividing the projections into odd and even angles.